Supplementary Information:
High-speed antiferromagnetic domain walls driven by coherent spin waves

Kyle L. Seyler, Hantao Zhang, Daniel Van Beveren, Costel R. Rotundu, Young S. Lee, Ran Cheng, and David Hsieh

Contents

1. Rotational anisotropy of SHG on a DW

Previous work showed that the SHG rotational anisotropy of $Sr_2Cu_3O_4Cl_2$ below $T_{N,I}$ can be described by a coherent superposition of electric quadrupole and magnetic dipole processes, which are sensitive to the crystallographic and magnetic order respectively [1]. We model the SHG rotational anisotropy pattern on a domain wall (DW) by the three-domain averaged intensity $I(2\omega,\phi) = \sum_{d=1,2,3} f_d |A\hat{e}_i^{\text{out}}\chi_{ijkl}^{\text{EQ}(i)}(\phi)\hat{e}_j^{\text{in}}q_k\hat{e}_l^{\text{in}} + A\hat{e}_i^{\text{out}}\chi_{ijk,d}^{\text{MD}(c)}(\phi)\hat{e}_j^{\text{in}}\epsilon_{klm}q_l\hat{e}_m^{\text{in}}|^2 I(\omega)^2$, where $\chi_{ijkl}^{\text{EQ}(i)}(\phi)$ is the i-type electric quadrupole susceptibility tensor transformed into the frame of the rotated scattering plane, $\chi_{ijk,d}^{\text{MD}(c)}(\phi)$ is the domain-dependent c-type magnetic dipole susceptibility tensor transformed into the frame of the rotated scattering plane, $\vec{q}$ the wavevector of incident light, $\hat{e}$ is the polarization of incoming fundamental or outgoing second-harmonic light, $I(\omega)$ is the intensity of the fundamental beam, A is a constant that depends on the polarization geometry, f_d accounts for the different domain fractions under the beam spot, and ϵ_{klm} is the Levi-Civita symbol. We first fit an SHG pattern from a single domain region (Fig. S1, top right, using $f_2 = f_3 = 0$) to extract the components for $\chi_{ijkl}^{\text{EQ}(i)}$ and $\chi_{ijk,1}^{\text{MD}(c)}$, which also gives $\chi_{ijk,2}^{\text{MD}(c)}$ and $\chi_{ijk,3}^{\text{MD}(c)}$ after 180° and 270° rotations respectively. We then fit the DW SHG pattern by only varying the relative domain intensities f_1, f_2, and f_3. As shown in Fig. S1, this process yields an excellent fit to our observed SHG pattern and demonstrates that the DW is Néel-type with $\mathbf{n}$ oriented along $-x$ at the DW center. When the laser is centered on the DW, we find that ∼20 % of the SHG intensity arises from the DW itself (and ∼40 % from each of the two antiphase domains). Because the SHG intensity scales with the square of the magnetization, this implies that the DW fills ∼26 % of the 40 µm diameter laser spot. The DW width can then be estimated as $0.26\pi(20\,\mu\text{m})^2/(40\,\mu\text{m}) \approx 8.2\,\mu\text{m}$, which is in excellent agreement with the ∼9 µm width extracted by directly fitting the DW profile.

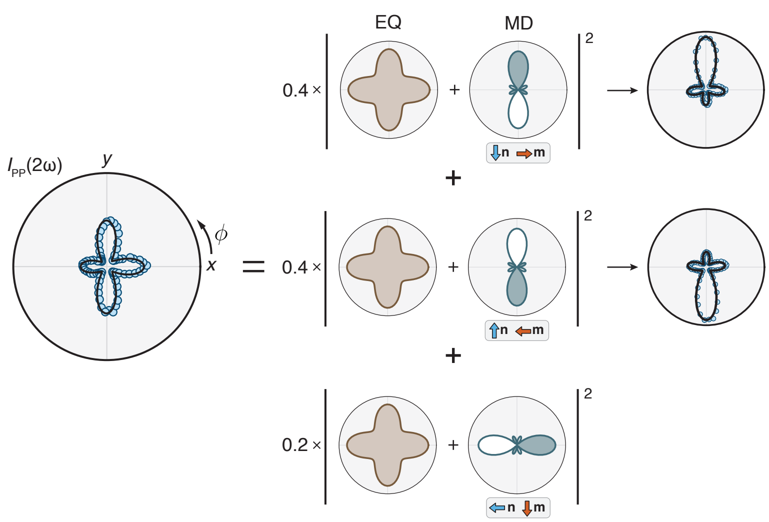

FIG. S1. SHG rotational anisotropy polar plot (with P-polarized input and output electric field polarization). The solid line is a fit to a three-domain averaged intensity, where each domain has SHG arising from a coherent superposition of electric quadrupole and magnetic dipole SHG processes, which are illustrated on the right. Filled and white lobes indicate opposite phase. The RA patterns on the right show the single domain data and fits.

2. Pump laser position dependence

Figure S2 shows how the light-induced DW motion depends on the position of the pump laser spot relative to the DW. For a fixed pump helicity, the DW always moves in the same direction, regardless of whether the pump laser spot is centered on the wall or spatially offset above or below it (Fig. S2a), which rules out simple laser heating effects as the underlying mechanism of DW motion. When the pump is offset from the DW, the DW motion is slightly more pronounced in the direction of higher pump intensity. This is not surprising since greater motion is expected with higher spin wave amplitude (Fig. S5). The asymmetry is also seen in the simulations (Fig. S7). However, if the pump beam does not directly excite the DW, as in Fig. S2b, we do not observe any motion. This suggests that the spin waves do not propagate appreciably outside of the pumped region.

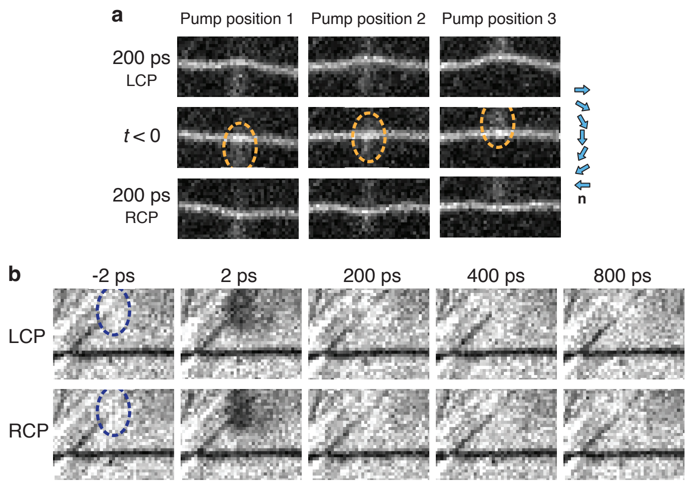

FIG. S2. **a**, SHG images of a DW for different pump laser positions (FWHM indicated by the dashed ovals). Images are displayed at $t < 0$ (center row) and $t = 200\,\mathrm{ps}$ for left (top row) and right (bottom row) pump circular polarization. The DW configuration (Néel vector orientations across the DW) is shown on the right. The vertical scale of each image is 20 µm. **b**, SHG images of an antiphase DW at different pump-probe time delays for left and right circular polarization when the pump laser is located completely off the DW. The SHG excitation polarization is orthogonal to the polarization used in **a**, so dark and bright regions are swapped. This allows one to clearly see the pumped region through the ultrafast melting of the magnetic order at $t = 2\,\mathrm{ps}$. The vertical scale of each image is 30 µm.

3. Pump scattering plane angle dependence

The inverse Faraday effect generates an effective magnetic field along the wavevector of circularly polarized pump light. For an oblique incidence pump pulse, this can create a transient in-plane magnetic field that couples to the weak in-plane magnetization of $Sr_2Cu_3O_4Cl_2$ and thereby induce DW motion. In this case, one would expect the DW motion to reverse with the opposite pump scattering plane angle. However, as shown in Fig. S3, for a given pump helicity, the DW always moves in the same direction, independent of the scattering plane angle. Therefore, the light-induced motion cannot arise from a transient in-plane opto-magnetic field.

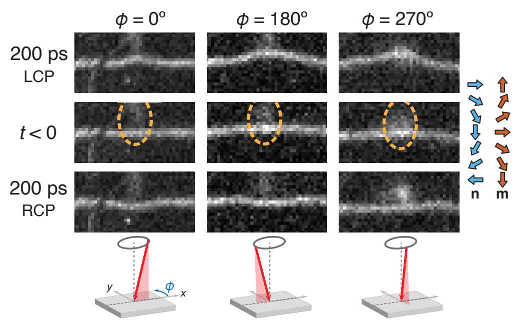

FIG. S3. **a**, SHG images of a DW for different pump laser scattering plane angles, $\phi = 0°$, $\phi = 180°$, and $\phi = 270°$ (schematically shown below each data column). Images are displayed at $t < 0$ (center row) and $t = 200\,\mathrm{ps}$ for left (top row) and right (bottom row) circular polarization. The angle of incidence is $\sim 10°$. The DW configuration, including the weak magnetic moments, is shown on the right. The vertical scale of each image is $20\,\mu\mathrm{m}$.

4. Motion under time-reversed configuration

Figure S4 shows that time-reversing the DW configuration (i.e., flipping all spins by 180°) does not affect the light-induced motion. The direction of the Néel vector and weak magnetic moment within the DW does not matter. Instead, the direction of light-induced wall motion is fully determined by the pump photon helicity and the sign of the DW winding number (whether the spins rotate clockwise or anti-clockwise across the wall).

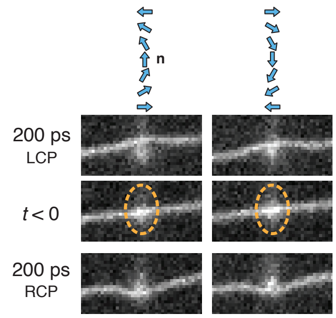

FIG. S4. SHG images of a DW for two different DW configurations, which are the time reversal of one another. Images are displayed at $t < 0$ (center row) and $t = 200\,\mathrm{ps}$ for left (top row) and right (bottom row) circular polarization. The vertical scale of each image is $20\,\mu\mathrm{m}$.

5. Pump fluence dependence

Figure S5 shows the extracted DW dynamics for two different pump fluences. In both the low and high fluence cases, the DW accelerates outward in the first ∼100 ps, then slows down and eventually reverses direction. The timescale of this outward acceleration, and the fact that it does not change with fluence, is consistent with our picture of light-induced spin waves driving the motion. The initial in-plane Néel vector rotation that occurs in the light-induced spin wave also occurs over ∼100 ps, as seen in Fig. 3e, and this spin wave frequency is not affected by the pump fluence. On the other hand, the spin wave amplitude increases with pump fluence, which explains why we observe an increase in the maximum DW position and maximum velocity when the fluence is increased. Further experimental studies are required to understand exactly how the DW velocity and maximum position scale with fluence. We note that the relationship may be complicated by the fact that higher pump laser fluence induces additional local heating that changes the DW energy landscape, which can affect the dynamics.

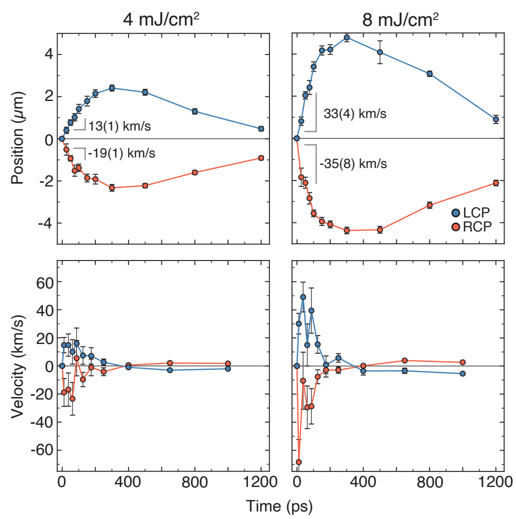

FIG. S5. Fitted position and velocity of the DW center (at the location of maximum movement) over time for different pump helicities at $4\,\mathrm{mJ/cm^2}$ (left two plots) and $8\,\mathrm{mJ/cm^2}$ (right two plots). The extracted velocity from a linear fit to the first 100 ps of data in the position-versus-time plots is also displayed. The DW was located in a different sample position compared to the data in Fig. 4. The pump laser was carefully centered on top of the DW so that changing the fluence did not shift the equilibrium DW position. The fit uncertainties are given as 1 standard deviation.

6. Additional DW dynamics simulations

Figure S6 shows DW dynamics simulations for different winding numbers and pump locations. In particular, comparing Fig. S6a (where $w = -1/2$) and Fig. S6b (where $w = 1/2$), we see that the dynamics are reversed for a chosen sign of $\dot{\phi}(t = 0)$. Furthermore, the effect of the pump laser position relative to the DW center is seen by comparing Fig. S6b, where the pump profile is positively offset from the DW, to Fig. S6c, where the pump profile is negatively offset from the DW. The direction of DW motion does not depend on the pump laser position, but the slight asymmetry between the $\dot{\phi}(t = 0) > 0$ and $\dot{\phi}(t = 0) < 0$ cases does. These findings are consistent with the experimental observations.

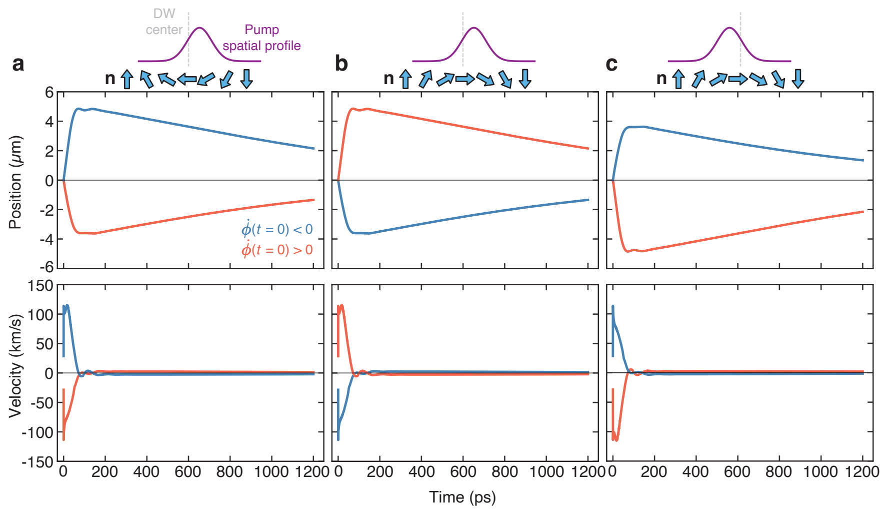

FIG. S6. **a**, Simulated time dependence of the DW position and velocity for $w = -1/2$ and pump position spatially offset to the right of the DW. **b**, Simulated time dependence of the DW position and velocity for $w = 1/2$ and pump position spatially offset to the right of the DW. **c**, Simulated time dependence of the DW position and velocity for $w = 1/2$ and pump position spatially offset to the left of the DW.

7. DW motion under spatially uniform pump

A spatially uniform rotation of spins merely shifts the global phase of a DW rather than shifting its position, as DW motion requires non-uniform spin rotation to accommodate the DW's inherent spatial inhomogeneity. This is seen in Fig. S7a, where we compare a DW at equilibrium and immediately after excitation by a uniform stimulus. Although the spins are out of equilibrium with a global phase shift, the DW center remains fixed at $x = 0$. This observation raises a fundamental question: how does DW motion emerge when subjected to a uniform stimulus, or more generally, when the pump's spatial profile is mismatched to the DW profile? To provide physical insight on this question, here we consider DW motion under the influence of spatially uniform stimulus as a simple case of spatial profile mismatch.

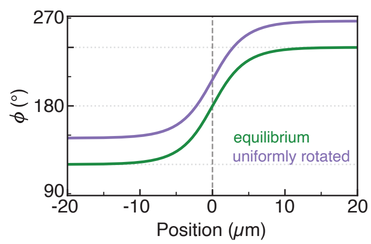

FIG. S7. Antiphase DW profile at equilibrium and after a uniform clockwise rotation of every spin.

To simplify the theoretical analysis without losing the essential physics, we drop the dissipation term, trapping potential, and coefficients before each term from the dynamical equation (Eq. (6) in the Methods section) and keep a minimal model for the DW:

$$\partial_t^2 \phi - \partial_x^2 \phi - \sin 2\phi = 0. \tag{1}$$

The static DW profile without stimulus, $\phi_0(x)$, is obtained by solving Eq. (1) with $\partial_t \phi = 0$, so it satisfies

$$\partial_x^2 \phi_0 + \sin 2\phi_0 = 0. \tag{2}$$

After the DW is exposed to stimulus, the DW profile can be decomposed as

$$\phi(x,t) = \phi_0(x) + \Delta\phi(x,t), \tag{3}$$

where $\Delta\phi(x,t)$ is a small stimulus-induced dynamical part on top of the static background. For a uniform stimulus, $\Delta\phi(x, t = 0) = \Delta\phi(t = 0) \equiv \Delta\phi(0)$ and $\partial_t \Delta\phi(x, t = 0) = \partial_t \Delta\phi(t = 0) \equiv \partial_t \Delta\phi(0)$, where $\Delta\phi(0)$ and $\partial_t \Delta\phi(0)$ serve as our initial conditions for Eq. (1). Substituting Eq. (3) into the dynamical equation (Eq. (1)) and noting that ϕ_0 is time-independent ($\partial_t^2 \phi_0 = 0$), we get

$$\partial_t^2 \Delta\phi - \partial_x^2 \phi_0 - \partial_x^2 \Delta\phi - \sin 2(\phi_0 + \Delta\phi) = 0. \tag{4}$$

For small $\Delta\phi$, we can perform a Taylor expansion of the sine term as $\sin 2(\phi_0 + \Delta\phi) \approx \sin 2\phi_0 + 2(\cos 2\phi_0)\Delta\phi$. Using Eq. (2), we therefore simplify Eq. (4) to:

$$\partial_t^2 \Delta\phi - \partial_x^2 \Delta\phi - 2(\cos 2\phi_0)\Delta\phi = 0. \tag{5}$$

At $t = 0$, since the stimulus is uniform, $\partial_x^2 \Delta\phi(t = 0) = 0$, then Eq. (5) becomes

$$\partial_t^2 \Delta\phi(t = 0) = 2(\cos 2\phi_0)\Delta\phi(0). \tag{6}$$

The left-hand side represents the "angular acceleration" of spins at $t = 0$ under the stimulus. The right-hand side is spatially non-uniform because the static DW profile $\phi_0(x)$ varies with position despite the uniform stimulus $\Delta\phi(0)$. Consequently, this non-uniform angular acceleration leads to a non-uniform rotation of the spins in the DW, which is ultimately necessary for the DW motion. This analysis does not contradict the previous statement that a spatially uniform rotation of spins cannot move a DW. Immediately after the initial stimulus, the DW center remains at $x = 0$, and it is the follow-up evolution that creates the required inhomogeneity.

In the case where $\Delta\phi(0) = 0$ but $\partial_t \Delta\phi(0) \neq 0$, we have $\partial_t^2 \Delta\phi(t = 0) = 0$ according to Eq. (6), meaning spins initially rotate uniformly without acceleration. However, after a small time Δt, $\Delta\phi(x, t = \Delta t) = \Delta t \times \partial_t \Delta\phi(0) \neq 0$ is still uniform, and we can repeat our analysis with the same result. This treatment is only valid at the beginning of the evolution and assumes a small stimulus relative to the DW profile.

To validate our understanding, we plot the simulated phase and angular velocity profiles after uniform and Gaussian pump excitation for the full dynamical equation in the main text (Fig. S8). While the initial angular velocity follows the profile of the pump pulse (either uniform or Gaussian), it develops additional inhomogeneity soon afterward, arising from the non-uniform angular acceleration of the spins due to the DW profile.

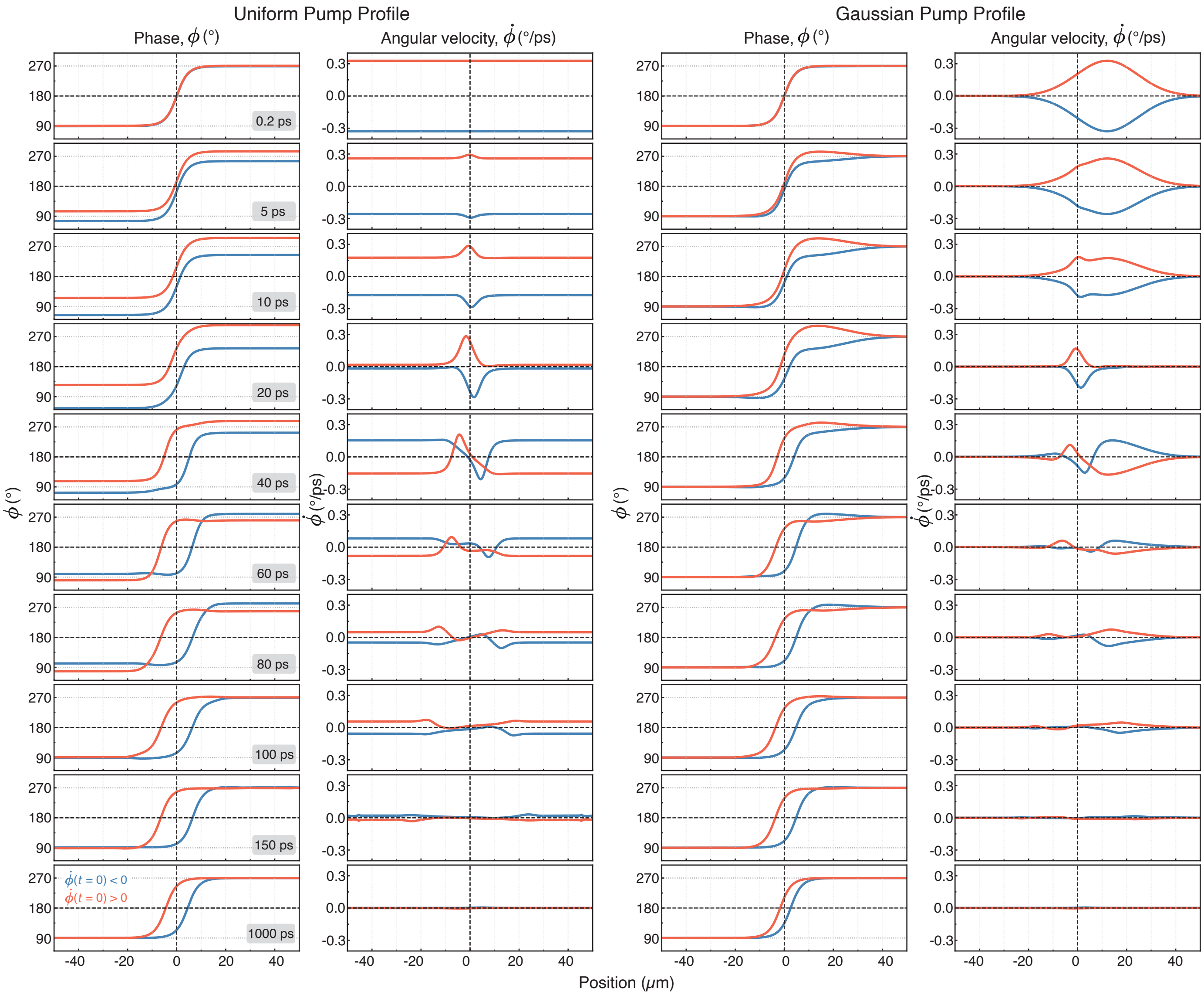

FIG. S8. Simulated time evolution of the DW phase and angular velocity profiles after excitation by a spatially uniform (left) or Gaussian (right) pump profile. The Gaussian pump case uses the same width and spatial offset as the other simulations in the text. For the uniform pump case, a top-hat pulse shape with 75 μm width was used. The simulation ranged from −100 μm to 100 μm. Each row corresponds to the same time indicated in the leftmost column.

* * *

[1] K. L. Seyler, A. Ron, D. Van Beveren, C. R. Rotundu, Y. S. Lee, and D. Hsieh, Direct visualization and control of antiferromagnetic domains and spin reorientation in a parent cuprate, Phys. Rev. B **106**, L140403 (2022).